ORIGINAL RESEARCH ARTICLE

Effect of Annealing Atmosphere and Steel Alloy Composition on Oxide Formation and Radiative Properties of Advanced High-Strength Steel Strip

KAIHSIANG LIN, MAEDEH POURMAJIDIAN, FATIMA K. SULEIMAN, JOSEPH R. MCDERMID, and KYLE J. DAUN

This study elucidates the effect of alloy composition, annealing atmosphere, and pre-annealed surface state on the radiative properties of dual-phase (DP) steels. Twelve samples of varying alloy composition and pre-annealed surface roughness were heated in a 95 pct/5 pct (vol) N_2/H_2 process atmosphere under dew points of + 10 °C and − 30 °C. The surface profile and surface topography were characterized using scanning electron microscopy and optical profilometry, while radiative properties were measured using a UV–Vis–NIR spectrophotometer and a Fourier transform infrared spectrometer. The surface oxide speciation and thickness were determined using X-ray photoelectron spectroscopy and focused ion beam milling, respectively. The results showed that smooth oxidized surfaces with lower Si/Mn mass ratios give rise to prominent interference effects observed in the measured reflectance. The thin-film interference model accurately predicts measured radiative properties. These findings can be used to improve the industrial pyrometry measurements in the continuous galvanizing line, and, potentially, to evaluate the oxide formation of DP steels during annealing *via in-situ* optical measurements.

https://doi.org/10.1007/s11663-021-02374-5

I. INTRODUCTION

ADVANCED high-strength steels (AHSS) are crucial for automotive light-weighting due to their higher strength and ductility compared to traditional high-strength low alloy (HSLA) steels. This allows automakers to manufacture vehicles with improved fuel efficiency, or longer range in the case of electric vehicles, without compromising passenger safety. However, AHSS are also more sensitive to temperature excursions during thermal processing, which can lead to substandard mechanical properties. Thermal excursions arising from pyrometer errors are principally due to wavelength-dependent variations in spectral emissivity caused by oxide formation during the annealing step of the CGL.[1]

Pyrometry relies on relating the detected spectral irradiance of a surface at one or more wavelengths to the surface temperature *via* Planck's distribution,

$$J_{\lambda,\mathrm{d}} \propto \varepsilon_{\lambda\mathrm{d}} I_{\lambda,\mathrm{b}}(\lambda_\mathrm{d}, T) = \frac{\varepsilon_{\lambda,\mathrm{d}} C_1}{\lambda_\mathrm{d}^5 \left[\exp\left(\frac{C_2}{\lambda_\mathrm{d} T}\right) - 1\right]} \approx \frac{\varepsilon_{\lambda,\mathrm{d}} C_1}{\lambda_\mathrm{d}^5 \exp\left(\frac{C_2}{\lambda_\mathrm{d} T}\right)}, \quad [1]$$

where $J_{\lambda,\mathrm{d}}$ is the detected spectral irradiance, $\varepsilon_{\lambda,\mathrm{d}}$ and $I_{\lambda,\mathrm{b}}$ are the spectral emissivity and blackbody intensity at the detection wavelength, respectively, $C_1 = 1.191 \times 10^8$ W μm^4/m^{2}sr, and $C_2 = 1.439$ μm K. In the case of two-wavelength pyrometry, surface temperature, T, is usually inferred from the ratio of spectral irradiances at two detection wavelengths, $J_{\lambda\mathrm{d}1}$ and $J_{\lambda\mathrm{d}2}$, which relies on $\varepsilon_{\lambda\mathrm{d}1}/\varepsilon_{\lambda\mathrm{d}2}$. The spectral-directional emissivity, $\varepsilon_\lambda(\theta)$, is related to the directional-hemispherical reflectance, $\rho_{\lambda,\mathrm{d\text{-}h}}(\theta)$, through Kirchhoff's law,

$$\varepsilon_\lambda(\theta) = 1 - \rho_{\lambda,\mathrm{d-h}}(\theta) \quad [2]$$

which is often required at normal or near-normal incidence for pyrometers measuring AHSS strip temperatures.

In the case of steel surfaces, $\varepsilon_{\lambda,\mathrm{d}1}/\varepsilon_{\lambda,\mathrm{d}2}$ changes continuously with oxide formation, which impacts both the surface phase chemistry and surface topography.[2] Accordingly, several studies have endeavored to

KAIHSIANG LIN, FATIMA K. SULEIMAN and KYLE J. DAUN are with the Department of Mechanical and Mechatronics Engineering, University of Waterloo, 200 University Ave. W, Waterloo, ON, N2L 3G1, Canada. Contact e-mail: kjdaun@uwaterloo.ca MAEDEH POURMAJIDIAN and JOSEPH R. MCDERMID are with the McMaster Steel Research Centre, McMaster University, 1280 Main Street W, Hamilton, ON, L8S 4L7, Canada.

Manuscript submitted June 21, 2021; accepted November 1, 2021. Article published online December 2, 2021.

elucidate the relationship between surface state and spectral emissivity in order to understand and, ultimately, correct for these effects.[3–5]

The type, location, and extent of oxidation depend on the chemical composition of the steel, the thermal processing history, and the annealing process atmosphere parameters. In particular, the dew point of the process atmosphere, *i.e.*, oxygen partial pressure (p_{O_2}), and alloy composition (*e.g.*, Si/Mn) play a significant role in determining the morphology and chemistry of the oxides that form during annealing. Selective oxidation occurs when, during annealing, the main alloying elements in steel, such as Mn and Si, segregate to the steel surface/subsurface and form external and/or internal oxides, respectively, depending on the p_{O_2} in the N_2–H_2 atmosphere. Samples annealed under a high dew point (*i.e.*, higher p_{O_2}) atmosphere tend to form internal oxides, while external oxidation tends to dominate when annealing under a lower dew point (*i.e.*, lower p_{O_2}) process atmosphere.[6] A variety of oxide morphologies, distributions, thicknesses, and chemistries have been reported across the family of AHSS alloys and process atmospheres in the literature. For example, in a study conducted on a transformation-induced plasticity (TRIP)-aided steel with Si/Mn = 0.34, thin-film external Mn–Si oxides were observed to form at low dew points, while at high dew points oxide nodules emerged on the steel surface.[7] Khondker *et al.*[6] studied how the oxidation potential of the annealing atmosphere influenced the selective oxidation of dual-phase steel alloyed with 2 wt pct Mn and 0.3 wt pct Mo. It was reported that Mn segregated to the surface and formed surface oxides under all experimental annealing atmospheres. The oxidation mode transitioned from external to internal when the oxidation potential of the atmosphere, *i.e.*, as p_{H_2O}/p_{H_2} increased from 8.44×10^{-3} to 3.451×10^{-2} (*i.e.*, p_{O_2} from 4.39×10^{-23} to 8.07×10^{-22} atm.). Bellhouse and McDermid[8] found that Mn, Si, and Al form external oxides when a 1.5 wt pct Al TRIP steel was annealed at 862 °C in N_2–H_2 atmospheres with p_{O_2} ranging between 5.08×10^{-25} and 2.80×10^{-19} atm. Using XPS and Auger electron microscopy, surface segregation of Si and Al was shown to be most significant under the lowest dew point of − 53 °C. Pourmajidian *et al.*[9] investigated the effect of oxygen partial pressure on the selective oxidation and oxide morphology of a 6 wt pct Mn, 2 wt pct Si third-generation advanced high-strength steels (3G-AHSS), and discovered considerable enrichment of Mn and Si in the form of oxides at the steel surface. They found that nodule-like external oxides formed during annealing at 690 °C under high dew point (+ 5 °C) as opposed to continuous film-like external oxides when annealing at lower dew points (− 50 °C, − 30 °C).

A number of studies have investigated how these different oxide states may influence radiative properties. Ham *et al.*[3] experimentally studied the effect of annealing atmosphere on selective oxidation and radiative properties of TRIP steel. The dew point strongly influenced oxide formation and measured spectral emissivity, and the effect of local surface texture induced by the oxide morphology on spectral emissivity was illustrated. More recently, Suleiman *et al.*[10] presented an empirical approach for modeling the spectral emissivity of dual-phase steels through factorial design-of-experiments. In their study, the variation of the measured spectral emissivity with alloy composition (Si/Mn = 0.04, Si/Mn = 0.10, Si/Mn = 0.23), pre-annealed surface state, and annealing dew point (− 30 °C, + 10 °C) was analyzed using full factorial designs. They found that alloy composition and pre-annealed surface state dominate the spectral emissivity at shorter (1.1 to 2.5 μm) and longer (2.5 to 5.0 μm) wavelengths, while annealing atmosphere has minor effect on measured spectral emissivity over the entire spectra.

In some scenarios, the presence of a thin oxide film on a smooth metal surface has been shown influence the spectral emissivity in a coherent way, as shown in Figure 1(a), because the reflections from the top and bottom interface of the oxide film induce a phase shift in the scattered electromagnetic (EM) wave, leading to constructive and destructive interference.[11,12] The extent of this effect depends on the film thickness relative to the EM wavelength, and may be significant when these two quantities are similar.[13] In contrast, EM waves become more sensitive to surface irregularities (*e.g.*, oxide nodules, surface roughness) when the wavelength becomes much larger than the oxide film thickness.[14] In this scenario, shown in Figure 1(b), the wave is scattered in a random way that can be predicted using geometric optics.[15] At longer wavelengths and shallow grazing angles, the wave/roughness interaction becomes dominated by diffraction effects.

Within the thin-film interference regime, many studies have shown that the spectral emissivity is sensitive to both annealing temperature and time as the oxide film grows. Brannon and Goldstein[5] experimentally investigated how total normal emissivity varies as a function of oxide thickness on a copper and aluminum substrate. Theoretical estimations of total normal emissivity based on interference wave optics were performed and compared to experimental results. While the theoretical estimations were lower than the measured values, they predicted the correct trend with respect to oxide layer thickness. Neuer and Guntert[16] showed that the spectral emissivity ($\lambda = 0.71$ μm) of an oxidized titanium surface oscillated as the oxide film grew until it plateaued once the film thickness exceeded 0.8 μm. Kobayashi *et al.*[17] investigated how the normal spectral emissivity of cold-rolled steel coupons varies with wavelength and time during annealing in vacuum and oxidizing environments. They found that the spectral emissivity oscillates with respect to wavelength at shorter wavelengths, and the peaks and the valleys in the oscillations caused by oxide film interference shifted to the longer wavelengths as the oxide became thicker.

Iuchi *et al.*[11] used a thin-film interference model to investigate the spectral emissivity of oxidized cold-rolled steels. Both predicted and measured results showed that the peaks and valleys in spectral emissivity shift to longer wavelengths with annealing time and increasing oxide film thickness. Likewise, when measuring the

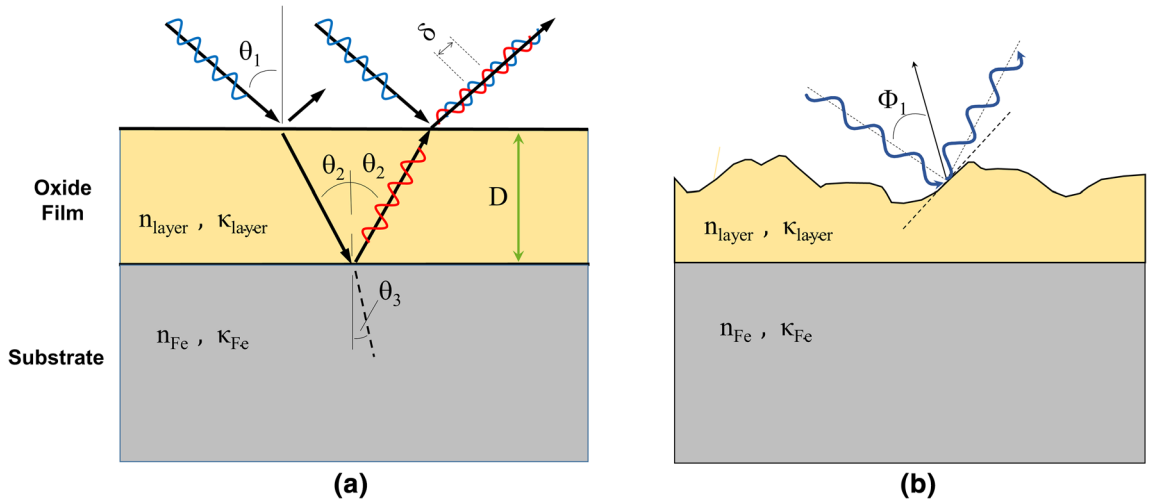

Fig. 1—Schematic view of the thin-film interference model where (*a*) an oxide layer is formed on the metal surface; (*b*) surface topography (*e.g.*, roughness) effect on EM wave scattering.

spectral emissivity of iron heated in air, Del Campo *et al.*[12] found that the peaks and valleys shift to longer wavelengths with the increase in annealing time. They later developed a quantitative model for the spectral emissivity that accounts for oxide film thickness, incident wavelength, and optical constants of the film.[18] King *et al.*[19] made similar observations on reactor pressure vessel alloys heated in air.

This study aims to elucidate the connection between the oxide formation, as determined by the alloy composition, annealing atmosphere oxygen potential, and the radiative properties of three dual-phase (DP) steel alloys, which is an important class of AHSS. Predictions are made through the thin-film interference model, which incorporates the measured refractive indices and film thickness of the oxides formed on steel substrate. Samples are obtained from three cold-rolled DP alloys, each having a different Si/Mn mass ratio (DP980-Si/Mn = 0.04, DP780-Si/Mn = 0.10, DP980-Si/Mn = 0.23). A subset of these samples are polished, and all the samples are annealed in a 95 pct/5 pct (vol) N_2/H_2 atmosphere at dew points of − 30 °C or + 10 °C using a galvanizing simulator (Iwatani-Surtec). Surface profiles are characterized by optical profilometry, as well as optical and scanning electron microscopy, while oxide composition is analyzed by X-ray photoelectron spectroscopy (XPS). *Ex-situ* directional-hemispherical reflectance measurements are carried out using a UV–Vis–NIR spectrophotometer (0.25 to 2.50 μm) and a Fourier transform infrared (FTIR) infrared spectrometer (2 to 20 μm), both equipped with integrating spheres. Near-normal specular reflectance measurements are also carried out using the FTIR spectrometer. Refractive indices and oxide film thicknesses are inferred through ellipsometry, while the oxide layer thickness is confirmed using a combination of focused ion beam (FIB) milling and scanning electron microscopy (SEM). These measurements are interpreted in the context of thin-film interference theory.

It is found that alloy composition, annealing atmosphere oxygen potential, and pre-annealed surface state strongly influence oxide formation and, therefore, the spectral emissivity of the specimens. Samples annealed in a polished state exhibited a stronger interference effect compared to those annealed in their as-received, cold-rolled condition. Reflectance predictions using the thin-film interference model are in line with the measurements over visible and near infrared wavelengths for most of the polished pre-annealed samples. These findings provide a potential means to estimate oxide formation *in-situ* through optical measurements during annealing, and can also be used to improve the pyrometry measurements carried out during the manufacturing process.

II. EFFECT OF ALLOY COMPOSITION AND ANNEALING ATMOSPHERE ON THE SELECTIVE OXIDATION OF AHSS

When AHSS alloys are annealed in a controlled dew-point (*i.e.*, controlled p_{O_2}) atmosphere, alloying elements segregate from the bulk material toward the surface and grain boundaries, forming oxides at the surface and in the subsurface of the steel. Since the annealing atmosphere is reductive with respect to the native oxide on the steel, FeO, this phenomenon is called *selective oxidation*.[7] This process depends on a variety of factors such as alloy composition, annealing temperature, and process atmosphere composition. Underlying the thermodynamic stability for metal/oxide equilibrium, the oxidation potential at a given temperature is determined by[18]

$$m\mathrm{M} + \frac{n}{2}\mathrm{O_2} \rightleftarrows \mathrm{M}_m\mathrm{O}_n\,(+\Delta G_1). \qquad [3]$$

The Gibbs free energy, ΔG_1, (J/mol), and the equilibrium constant, K_1, of this reaction at annealing temperature, T (K), can be written as

$$\Delta G_1 = -\mathrm{RT}\ \ln K_1 \quad [4]$$

$$K_1 = \frac{\alpha_{\mathrm{M}_m\mathrm{O}_n}}{\alpha_{\mathrm{M}}^{m}\, p_{\mathrm{O}_2}^{n/2}} = \frac{1}{\alpha_{\mathrm{M}}^{m}\, p_{\mathrm{O}_2}^{n/2}}, \quad [5]$$

where R is the universal gas constant, $R = 8.314$ J/(mol K). The oxide is assumed to be a pure condensed species with an activity of unity ($\alpha_{\mathrm{M}_m\mathrm{O}_n} = 1$), and α_{M}^{m} denotes the atomic fraction of species M in the alloy.

With a fixed hydrogen content at a given T, the oxygen potential of the process atmosphere, p_{O_2} (atm), is determined by the partial pressures of water vapor, $p_{\mathrm{H}_2\mathrm{O}}$, and hydrogen, p_{H_2}, in the atmosphere[18]

$$\mathrm{H}_2 + \frac{1}{2}\mathrm{O}_2 \rightleftarrows \mathrm{H}_2\mathrm{O}\ (\mathrm{g})\ (+\Delta G_2) \quad [6]$$

$$\Delta G_2 = -\mathrm{RT}\ \ln K_2 \quad [7]$$

$$K_1 = \frac{p_{\mathrm{H}_2\mathrm{O}}}{p_{\mathrm{H}_2}\, p_{\mathrm{O}_2}^{1/2}}, \quad [8]$$

where p_{H_2} is 0.05 in the case of a 95 pct/5 pct N_2/H_2 atmosphere and $p_{\mathrm{H}_2\mathrm{O}}$ is determined by the process atmosphere dew point, T_{dp}, which is the temperature at which the liquid water–water vapor reaction is at equilibrium,

$$\mathrm{H}_2\mathrm{O}\ (\mathrm{l}) \rightleftarrows \mathrm{H}_2\mathrm{O}\ (\mathrm{g})\ (+\Delta G_3) \quad [9]$$

$$\Delta G_3 = -\mathrm{RT}_{\mathrm{dp}}\ \ln(p_{\mathrm{H}_2\mathrm{O}}), \quad [10]$$

where liquid water is assumed to be a pure condensed species, *i.e.*, $\alpha_{p\mathrm{H}_2\mathrm{O}} = 1$.

The Gibbs energy for each compound can be approximated using[20]

$$\Delta G = AT\ln(T) + BT + CT^2 + DT^{-1} + ET^{1/2} + F \times 10^{-7}T^3 + G \quad [11]$$

where coefficients A, B, C, D, E, F, G corresponding to each compound are listed in Table I.

Consequently, the curves of oxygen potential for each oxide and for a given atmospheric condition with respect to the annealing temperature can be derived using Eqs. [3] through [11], as depicted in Figure 2. If the atmospheric oxygen potential at a given temperature and dew point exceeds the equilibrium oxygen potential of a specific compound, the oxide will form since the oxygen potential in the environment is greater than the equilibrium oxygen partial pressure of species M. As shown in Figure 2, when the alloy is annealed with either dp = − 30 °C or dp = + 10 °C, the atmospheric oxygen potentials exceeds those of Mn and Si oxides (Additional curves corresponding to ternary oxides, *i.e.*, $MnSiO_3$ and Mn_2SiO_4, exist in the shaded area between the MnO and SiO_2 curves but are not shown). In this scenario, Mn, Si, and possibly Cr could form stable oxides, while FeO is less likely to form on the metal substrate. It should be remembered that these calculations are based on thermodynamic equilibrium between the substrate and the atmosphere and do not account for the kinetics of segregation of the alloying elements, which can cause the oxide layer composition to vary with time and location.

The selective oxidation of DP AHSS during intercritical annealing has been investigated extensively as described in References 8, 9 and 22–29. These works show that annealing atmosphere and Si/Mn ratio strongly influence the chemistry and morphology of oxides that form during intercritical annealing. Suzuki *et al.*[30] interpreted the selective oxidation behavior of Si and Mn using a thermodynamic equilibrium calculation based on the chemical potential of the Fe–Mn–Si–O system. Their model showed that, in alloys with a Si/Mn ratio below 0.5, formation of SiO_2 as the dominant surface oxide species could be avoided when annealing under conventional, dew-point-controlled process atmospheres. In this scenario, Mn-rich oxides, such as MnO, tend to form on the surface under high process atmosphere dew points, while ternary oxides, *e.g.*, $MnSiO_3$ and Mn_2SiO_4, become prevalent at lower dew points. It was also found that as the Si/Mn ratio increases, the oxide species gradually transform from Mn-rich oxides to ternary oxides and SiO_2.

Seyed Mousavi *et al.*[22] studied the selective oxidation of a 2 wt pct Mn, 1.3 wt pct Si AHSS having a Si/Mn ratio of 0.64 during annealing heat treatments at 820 °C. It was found that the external oxides consisted of film-like $MnSiO_3$, Mn_2SiO_4, SiO_2, and nodule-like MnO at the outermost layer when the samples were annealed with dp = − 50 °C atmosphere, while nodule-like $MnSiO_3$, Mn_2SiO_4, and MnO were formed among the external surface region when the samples were annealed in a dp = + 10 °C atmosphere. Further work by Seyed Mousavi *et al.*[23] was carried out on the effects of dew point (− 50 °C, − 30 °C, + 5 °C), and Sn as a micro-addition on the selective oxidation of a 2 wt pct Mn, 1.7 wt pct Si AHSS having a Si/Mn ratio of 0.87 during annealing heat treatments at 840 °C. They found that the thickness of the external oxides formed at lower dew points was smaller than those formed at a higher dew point. The external oxides consisted of MnO, while internal oxide networks comprised $MnSiO_3$ and SiO_2 for both the bulk internal and grain boundary oxides. Pourmajidian and McDermid[31] investigated the effect of annealing atmosphere (− 50 °C, − 30 °C, + 5 °C) on the selective oxidation of a 3G-AHSS model alloy with Si/Mn = 0.32 during annealing heat treatments at 800 °C. The measured external oxide thicknesses varied between 40 and 300 nm across different dew points and soaking times, and the outermost external oxide layer was found to be MnO for all process atmospheres. Surface oxides formed under a T_{dp} = − 50 °C atmosphere consisted of a layered configuration of SiO_2, $MnSiO_3$, and MnO, while the oxides formed under a + 5 °C dew point only comprised nodule-like MnO. Similar findings were reported at a

Table I. Corresponding Coefficients Used to Obtain the Gibbs Energy for Each Compound via Eq. [11], Derived From Ref. [20]

Compound	A (J/mol K)	B (J/mol K)	C (J/mol K^2)	D (J/mol K^{-1})	E (J/mol $K^{0.5}$)	F (J/mol K^3)	G (J/mol)
FeO (s)	− 312.37974	2289.59246	0.1296543	35023345.2	1042.28461	5.85664	− 536965.33
MnO (s)	1.3662852	36.6929348	0.00481023	352614.968	1042.28461	− 3.9889179	− 395773.02
SiO_2 (s)	8.21930022	79.2570095	− 0.0009297	1322689.18	2084.56922	− 1.1798608	− 932891.64
Cr_2O_3 (s)	297.799334	− 2306.3214	− 0.1006328	4175977.18	23712.6364	119.406	− 1292002.1
H_2O (l)	− 2304.0466	18256.7583	1.4416257	− 8161063.5	− 121879.48	− 3158.67	245617.101
H_2O (g)	14.5914916	− 49.440744	− 0.0053297	− 122643.5	− 76.542088	3.47762	− 236434.09

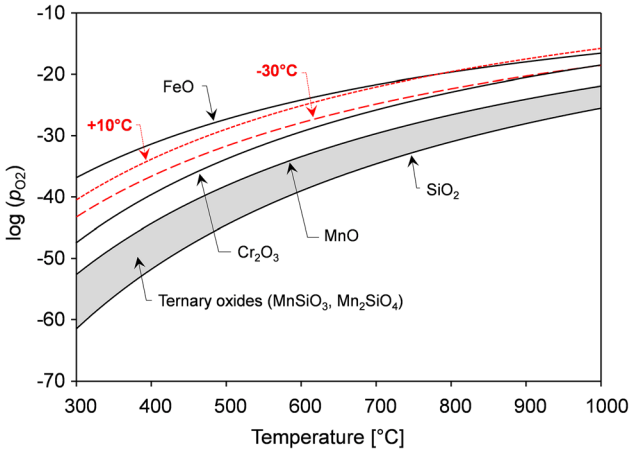

Fig. 2—Thermodynamic stability of oxygen potential (in logarithmic scale) with respect to annealing temperature. (p_{O_2} in atm.) The curves are calculated and derived based on the Gibbs energy equations of FeO, MnO, SiO_2, and Cr_2O_3 formation.[21] Curves of the dew points (− 30 °C and + 10 °C) shown in red dashed lines are derived underlying 95 pct/5 pct N_2/H_2 atmosphere, while curves corresponding to Mn–Si ternary oxides (*e.g.*, $MnSiO_3$, Mn_2SiO_4) exist in the gray shaded area between the curves of MnO and SiO_2, but are not shown in the plot. Note that the metallic oxide curves are calculated based on the alloy compositions of the present study (Color figure online).

lower annealing temperature of 690 °C,[9] where the external oxides were MnO and the internal oxide networks comprised a multi-layered structure of $MnSiO_3$ surrounding a SiO_2 core. Alibeigi *et al.*[32] found that only MnO appears on the external surface of high Mn (Si/Mn < 0.06) steels annealed under different dew points (− 50 °C, − 30 °C, − 10 °C, + 5 °C) at annealing temperatures range from 630 °C to 770 °C. The external oxide thickness was below 100 nm in all cases. Oh *et al.*[33] investigated the oxide formation on a 1.64 wt pct Mn, 1.48 wt pct Si TRIP steel (Si/Mn = 0.9) annealed at 820°C under a dew point of – 60 °C. It was found that a thick Mn-rich oxide layer was formed on the surface and Si-rich oxides were formed in the subsurface region. The thickness of the Mn-rich oxide layer ranged from 20 to 50 nm, while the thickness of the Si-rich oxide layer was found to be less than 20 nm. A summary of these studies with respect to the alloy composition, annealing conditions, and oxide formations is presented in Table II.

Based on these studies, surface oxides of the samples investigated in present study (Si/Mn = 0.04, Si/Mn = 0.10, Si/Mn = 0.23) are likely to consist of Mn-rich oxide or Si–Mn ternary oxides depending on the annealing dew point and alloy Si/Mn ratio. For the alloy having the lowest Si/Mn ratio (Si/Mn = 0.04), the oxide layer is likely to consist of MnO under both annealing dew points considered in this study (− 30 °C, + 10 °C). Ternary oxides including $MnSiO_3$ and Mn_2SiO_4 may form alongside MnO on the other two alloys (Si/Mn = 0.10, Si/Mn = 0.23). This is because for low Si/Mn alloy, large amount of Mn tends to segregate onto the surface and form Mn-rich oxides during annealing, while ternary oxides would appear on the surface for high Si/Mn alloy as more Si is available to segregates from the bulk onto the surface during annealing.

The oxide species of these samples will also be examined using XPS.

III. OXIDE FILM INTERFERENCE EFFECT

Consider the scenario of an oxide film of thickness D and uniform composition forming on a smooth metal surface. If the wavelength of an incident EM wave is comparable to the oxide film thickness ($\lambda \sim D$), Figure 1(a), the film causes a phase shift, leading to oscillations in the spectral reflectivity with respect to wavelength[11] that depend on the complex refractive index of the oxide film, $\tilde{n}_2 = n_2 + ik_2$, and the substrate steel, $\tilde{n}_3 = n_3 + ik_3$. (The refractive index of air is $n_1 = 1$.) Maxwell's equations can be solved to obtain the vertical and parallel-polarized reflectances (also known as Airy's formula[34]) as follows:

$$\rho_v(\lambda) = \left| \frac{\eta_{12v} + \eta_{23v}\exp(-i\zeta)}{1 + \eta_{12v}\eta_{23v}\exp(-i\zeta)} \right|^2, \qquad \rho_p(\lambda) = \left| \frac{\eta_{12p} + \eta_{23p}\exp(-i\zeta)}{1 + \eta_{12p}\eta_{23p}\exp(-i\zeta)} \right|^2, \quad [12]$$

where the reflectance parameters, η_{12v}, η_{23v}, η_{12p}, η_{23p}, at the interfaces are expressed by

$$\eta_{12v} = \frac{n_1\cos\theta_1 - \tilde{n}_2\cos\theta_2}{n_1\cos\theta_1 + \tilde{n}_2\cos\theta_2}, \quad \eta_{23v} = \frac{\tilde{n}_2\cos\theta_2 - \tilde{n}_3\cos\theta_3}{\tilde{n}_2\cos\theta_2 + \tilde{n}_3\cos\theta_3} \quad [13]$$

$$\eta_{12p}=\frac{\tilde{n}_2\cos\theta_1 - n_1\cos\theta_2}{\tilde{n}_2\cos\theta_1+n_1\cos\theta_2}, \quad \eta_{23p}=\frac{\tilde{n}_3\cos\theta_2 - \tilde{n}_2\cos\theta_3}{\tilde{n}_3\cos\theta_2+\tilde{n}_2\cos\theta_3}, \quad [14]$$

and

$$\zeta = \frac{4\pi\tilde{n}_2 D\cos\theta_2}{\lambda} \quad [15]$$

is the phase difference of reflected wave. The incident angle, θ

$_1$, is taken to be 10 deg (the angle of incidence for the spectrophotometer and spectrometer) and is related to θ_2 and θ_3 by Snell's law

$$n_1 \sin\theta_1 = \tilde{n}_2 \sin\theta_2 = \tilde{n}_3 \sin\theta_3. \quad [16]$$

In the case of unpolarized incident radiation, the specular reflectance can then be obtained from $\rho_\lambda = [\rho_v(\lambda) + \rho_p(\lambda)]/2$, and, since emission is always unpolarized, $\varepsilon_\lambda = 1-\rho_\lambda$. The substrates of all the samples are modeled as ferrite, with refractive indices from Reference 35. The refractive indices of MnO are derived from Reference 36. Figure 3 shows the literature-derived refractive indices of ferrite and MnO. In present study, the refractive indices of other ternary oxides that are likely to form on the substrate, as discussed in Section II, are obtained through the ellipsometry measurements, since they are unavailable from the literature. Figure 4 shows that the measured spectral reflectance for all three alloys with polished surfaces closely matches predictions made using Fresnel's equation with refractive indices of iron shown in Figure 3. Consequently, it is reasonable to model substrate alloys as ferrite.

IV. SAMPLE PREPARATION AND MEASUREMENTS

Table III lists the two cold-rolled DP980 alloys (alloys A1 and A2) and one cold-rolled DP780 alloy (alloy A3) used in the present study. All alloys have elemental compositions consistent with ASTM standard A1079-17.[37] Experimental conditions of the twelve samples analyzed in this study are shown in Table IV. 120 mm × 200 mm panels were cut from coils of cold-rolled DP980 and DP780. In order to investigate the influence of the pre-annealed surface state on oxide formation and radiative properties, half of the samples were annealed in their as-received state, while the other half were polished using a series of SiC polishing papers with progressively finer grit and particle size (240, 320, 400, 600 grit), resulting in a mirror finish with identical roughness levels (σ = 0.09 μm) obtained using an optical profilometer (WYKO NT1100). The coupons were then annealed in a galvanizing simulator (Iwatani-Surtec) using a 95 pct/5 pct N_2/H_2 atmosphere and dew points of either + 10 °C or – 30 °C, corresponding to oxygen partial pressures of 2.56×10^{-20} atm (pH_2O/pH_2: 0.2408) and 4.39×10^{-23} atm (pH_2O/pH_2: 0.00998), respectively. The samples were heated according to the heating schedule illustrated in Figure 5. The surfaces of the processed coupons were imaged using an optical microscope (×50). All samples were cleaned and rinsed with ethanol and acetone prior to microscopy analysis. FIB milling in combination with SEM analysis was carried out using an NVision 40 FIB-SEM microscope (Zeiss) to image the steel cross-sections using secondary electron imaging (SEI). The surface oxide thickness of all samples were measured using ImageJ 1.48v software and the results are listed in Table IV, where the error bars represent the margin of error at 95 pct confidential interval of the mean. Further details of this procedure can be found in Reference 31.

X-ray photoelectron spectroscopy was performed using a PHI Quantera II scanning XPS microprobe to obtain the surface oxide speciation of selected samples. The X-ray beam diameter was 100 μm and the take-off angle was set at 45 deg. High-resolution spectra of the Mn2p and Mn3s peaks were collected with a pass energy and step size of 26 eV and 0.1 eV, respectively, and 112 and 0.2 eV for the Si2p. All data processing were performed using MultiPak software and the binding energies of the aforementioned peaks were used to speciate the surface oxides, shown in Table IV.

The near-normal directional-hemispherical spectral reflectance of each coupon was measured using a Varian Cary 5000 UV–Vis–NIR spectrophotometer (0.25 to 2.5 μm) and a Bruker Invenio-R spectrometer (2.5 to 20 μm). Refractive indices and thickness of the oxide films formed on the substrate were measured using a J. A. Woollam M-2000 ellipsometer (400 to 750 nm).

V. RESULTS AND DISCUSSION

The surface roughness and surface slope of the polished samples are both smaller compared to those of the as-received samples, as shown in Table IV. The oxide thicknesses measured using ellipsometry are consistent with those obtained *via* the FIB-SEM methodology. The alloy composition, process atmosphere, and pre-annealed surface topography significantly influence the oxide thickness formed during annealing. For samples annealed at dp = – 30 °C, thicker oxides are obtained on as-received samples, while for samples annealed at dp = + 10 °C, thicker oxides are found on polished samples except for the case of the high Si/Mn ratio alloy (Si/Mn = 0.23).

Furthermore, XPS analysis showed that the dominant surface oxide species at dp = – 30 °C is Mn_2SiO_4, with the exception of sample 3 where MnO was identified as the primary oxide, which is consistent with the observation that this alloy had the lowest Si/Mn ratio, *i.e.*, 0.04. For the steels that were annealed under the + 10 °C dew-point atmosphere, MnO was the main surface oxide, except for sample 11 which also has the highest Si/Mn ratio of 0.23. These observations are in agreement with the previous findings[30–33] which were discussed in Section II.

Surface microstructure and topographical images of the samples are shown in Figure 6. The as-received surfaces are rougher and exhibit rolling artifacts. For the polished surfaces having the lowest Si/Mn ratio (Si/

Table II. Summary of the Oxide Formations Subject to Annealing Conditions From Relevant Literatures

Ref No.	Si/Mn (Wt pct)	Annealing Temperature (°C)	Atmospheric Dew Point, T_{dp} (°C)	Oxygen Potential, p_{O_2} (atm)	Oxide Thickness, D (nm)	Surface Oxide Species	Oxide Morphology
[22]	0.64	820	− 50 − 30 + 5	1.96×10^{-24} 1.21×10^{-22} 3.45×10^{-20}	—	dp = − 50 °C, − 30 °C: MnO, $MnSiO_3$, $MnSiO_4$, SiO_2; dp = + 5 °C: MnO, $MnSiO_3$, $MnSiO_4$;	dp = − 50 °C, − 30 °C: film-like; dp = + 5 °C: nodular
[23]	0.87	840	− 50 − 30 + 5	5.52×10^{-24} 3.41×10^{-22} 9.68×10^{-20}	20 to 100 nm	MnO, $MnSiO_3$, SiO_2	dp = − 50 °C, − 30 °C: film-like; dp = + 5 °C: nodular
[25]	0.65 1.0	797, 777	− 50 − 30 + 5	4.13×10^{-26} 4.05×10^{-23} 1.41×10^{-20} 7.16×10^{-27} 1.40×10^{-23} 3.95×10^{-21}	—	MnO, $MnSiO_4$, SiO_2	dp = − 50 °C, − 30 °C: widely spaced nodules; dp = + 5 °C: closely spaced nodules;
[28]	0.64	820	− 60 − 10 + 5	1.29×10^{-26} 7.38×10^{-22} 8.33×10^{-21}	dp = − 60 °C: 30 to 40 nm; dp = + 5 °C: 5 nm	MnO, $MnSiO_3$, $MnSiO_4$, SiO_2	dp = − 60 °C: film-like; dp = − 10 °C, + 5 °C: fine-grained;
[29]	0.64	820	− 60 − 30 − 10 0 + 5	1.29×10^{-26} 1.58×10^{-23} 7.38×10^{-22} 4.09×10^{-21} 8.33×10^{-21}	—	dp = − 60 °C: MnO, $MnSiO_3$, $MnSiO_4$, SiO_2; dp = − 30 °C: $MnSiO_3$, $MnSiO_4$, SiO_2; dp = − 10 °C: $MnSiO_3$, $MnSiO_4$, SiO_2; dp = 0 °C: $MnSiO_3$, $MnSiO_4$; dp = + 5 °C: $MnSiO_3$, $MnSiO_4$;	dp = − 60 °C, − 30 °C: film-like; dp = 0 °C, + 5 °C: nodules;
[31]	0.32	800	− 50 − 30 + 5	6.87×10^{-25} 4.39×10^{-23} 1.29×10^{-20}	40 to 300 nm	dp = − 50 °C , − 30 °C: MnO, $MnSiO_3$, SiO_2; dp = + 5 °C: MnO, $MnSiO_3$;	dp = − 50 °C , − 30 °C: film-like; dp = + 5 °C: nodular
[32]	0.005 to 0.064	630, 685, 724, 750, 770;	− 50 − 30 − 10 + 5	2.05×10^{-29} $- 2.62 \times 10^{-21}$	5 to 35 nm (Si/Mn = 0.05) 30 to 80 nm (Si/Mn = 0.064) 35 to 95 nm (Si/Mn = 0.015) 38 to 65 nm (Si/Mn = 0.005) 55 to 95 nm (Si/Mn = 0.01)	MnO	dp = − 50 °C , − 30 °C , − 10 °C: film-like; dp = + 5 °C: nodular
[33]	0.90	820	− 60	1.71×10^{-25}	20 to 50 nm (Mn-rich) 0 to 20 nm (Si-rich)	MnO, $MnSiO_3$, $MnSiO_4$, SiO_2	film-like

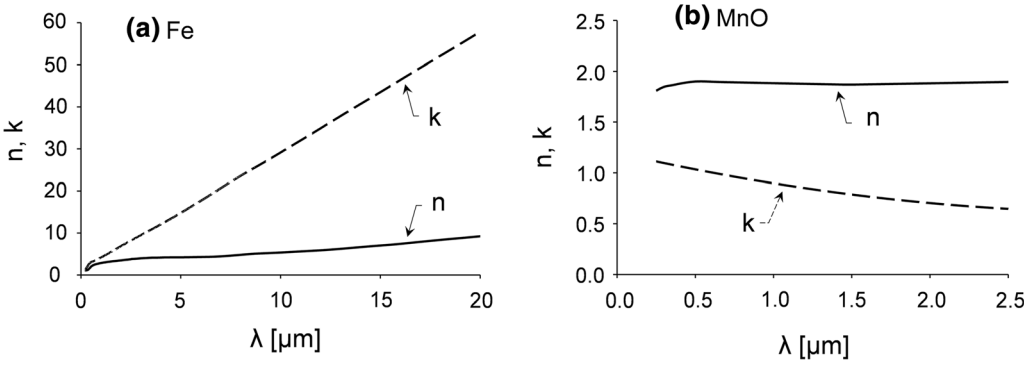

Fig. 3—Refractive indices of (*a*) ferrite[35] and (*b*) MnO.[36]

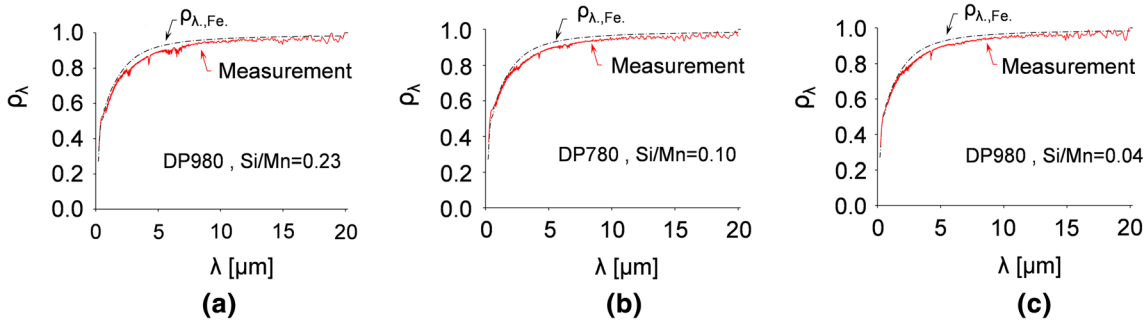

Fig. 4—Comparison of measured reflectances of polished surfaces for different alloys: (*a*) DP980, Si/Mn = 0.23; (*b*) DP780, Si/Mn = 0.10; and (*c*) DP980, Si/Mn = 0.04. The surfaces of the samples were polished to the same roughness scale (σ = 0.09 μm) before the measurements. The dashed lines denote the reflectance of ferrite derived using Fresnel's equation with refractive indices from Ref. [35].

Mn = 0.04), the one annealed at the higher dew point (sample #9) is rougher than the one annealed at the lower dew point (sample #3), while the opposite trend holds for alloys having a higher Si/Mn ratio.

The colors of samples having different alloy compositions (Si/Mn ratio) and pre-annealed surface topography are distinct from each other, while samples having identical Si/Mn ratio and pre-annealed surface condition have a similar color. This implies that alloy composition and surface topography have a stronger effect on radiative properties of AHSS in the visible spectra compared to that of the annealing atmosphere, which is consistent to what has been found in Reference 10.

This observation is also borne out in the reflectance measurements shown in Figure 7, where the curves corresponding to samples having identical Si/Mn and pre-annealed surface state are generally similar over the visible spectra. In addition, the measured reflectances of samples annealed in their as-received state are generally higher among the visible spectra compared to those of the polished samples. These results are consistent with the brighter images of as-received surfaces shown in Figure 6.

Given the measured surface oxide thickness scale (50 to 115 nm) of all the samples, the radiative properties should be influenced by both oxide film and surface topography effects across the UV–Vis–NIR wavelengths.[38,39] The interference effect is particularly distinct for coupons annealed in the polished state, and especially for low Si/Mn alloys. This is likely due to the fact that, for polished surfaces, the oxide grows more uniformly across the smooth substrate, leading to a more coherent wave interference effect and a lower reflectance over the visible spectra. Conversely, the reflectance of coupons annealed in their as-received state exhibits less oxide film interference. As the oxide film thickness increases, the interference effect shifts to longer wavelengths; this is particularly pronounced when comparing the reflectances of sample #3 and sample #9, where the minimum point of the curve shifts to longer wavelengths as the oxide thickness increases from 70 to 110 nm.

Figure 8 shows SEM cross-sections of sample #1, #5, #7, #11, highlighting the effect of alloy composition and annealing dew point on the oxide structure. Sample #1 (Si/Mn = 0.10, annealed at – 30 °C) has a uniform, continuous oxide film, while isolated oxide nodules are found on sample #5 (Si/Mn = 0.23, annealed at – 30 °C) and sample #11 (Si/Mn = 0.23, annealed at + 10 °C). The oxides on sample #7 (Si/Mn = 0.10, + 10 °C) have a semi-continuous film-like appearance, while the ones observed on the surface of sample #11 are isolated nodules (Si/Mn = 0.23, + 10 °C). The oxides formed on samples #3 and #9 (Si/Mn = 0.04) where film-like and more comparable to those of the Si/Mn = 0.1 alloy.

Table III. List of Tested AHSS Alloys With Chemical Compositions (Wt Pct) Based on the ASTM Standards (A1079-17).[37] The Si/Mn Ratio is Measured Using Inductively Coupled Plasma Spectroscopy

Alloy	C	P	S	Cu	Ni	Cr + Mo	Mn + Al + Si	Si/Mn
DP980 (A1)	0.23	0.08	0.015	0.20	0.50	1.40	6.00	0.23
DP980 (A2)	0.23	0.08	0.015	0.20	0.50	1.40	6.00	0.04
DP780 (A3)	0.18	0.08	0.015	0.20	0.50	1.40	5.40	0.10

Table IV. Tested Samples With Different Alloy Compositions, Annealing Atmospheres, Measured Pre-annealed and Post-annealed Roughness, and Measured Oxide Thickness and Oxide Species

Sample No.	DP (°C)	Si/Mn	Pre-annealed Surface State	σpre (μm)	σpost (μm)	σ/τ (post)	Oxide Thickness (nm) Ellip.	Oxide Thickness (nm) FIB	Primary Oxide (XPS)
1 (A3)	− 30	0.10	polished	0.09	0.26	0.04	58.5	53.4 ± 2.9	Mn_2SiO_4, Cr_2O_3, MnO
2 (A3)	− 30	0.10	as-received	2.60	2.73	—	—	62.5 ± 3.8	—
3 (A2)	− 30	0.04	polished	0.09	0.17	0.03	70.7	67.4 ± 3.2	MnO, Cr_2O_3, $MnSiO_3$
4 (A2)	− 30	0.04	as-received	0.65	0.71	—	—	91.2 ± 5.1	—
5 (A1)	− 30	0.23	polished	0.09	0.28	0.04	74.1	70.5 ± 5.8*	Mn_2SiO_4, Cr_2O_3, MnO
6 (A1)	− 30	0.23	as-received	0.59	0.67	—	—	63.8 ± 6.1*	—
7 (A3)	+ 10	0.10	polished	0.09	0.21	0.04	112.8	101.7 ± 7.1	MnO, Mn_2SiO_4
8 (A3)	+ 10	0.10	as-received	2.60	3.10	—	—	84.7 ± 9.0	—
9 (A2)	+ 10	0.04	polished	0.09	0.27	0.05	110.6	114.5 ± 7.9	MnO, $MnSiO_3$
10 (A2)	+ 10	0.04	as-received	0.65	0.56	—	—	103.8 ± 6.3	—
11 (A1)	+ 10	0.23	polished	0.09	0.25	0.04	68.0	65.3 ± 6.6*	Mn_2SiO_4, MnO
12 (A1)	+ 10	0.23	as-received	0.59	0.72	—	—	94.4 ± 12.1*	—

*These measured thickness values contain significant nodule-like oxides as opposed to film-like oxides at the external surface region.

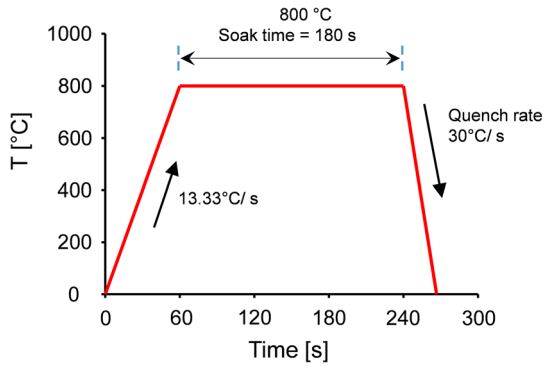

Fig. 5—Annealing schedule for the tested coupons. The coupons were heated to 800 °C and soaked for 180 s before quenching.

In general, samples with Si/Mn = 0.23 form nodule-like oxides. On the other hand, the effect of dew point on oxide morphology was less pronounced, and oxide thickness and chemistry were more affected by this process parameter depending on the alloy composition.

Figure 9 shows the measured refractive indices for the oxide films obtained from ellipsometry. It can be seen that the measured refractive indices between the samples annealed with dp = − 30 °C and dp = + 10 °C are similar for the low Si/Mn alloy (Si/Mn = 0.04, sample #3 and #9), and the measured values are close to that of MnO. This is in line with the XPS results of sample 3 (Table II), which indicate that the surface oxides are mainly MnO, with minor $MnSiO_3$ and Cr_2O_3 as one would expect for low Si/Mn alloys. For the alloys of the intermediate Si/Mn ratio (Si/Mn = 0.1, sample #1 and #7), the measured refractive indices are sensitive to the dew point and are different from that of MnO. For the two samples having the highest Si/Mn ratio (Si/Mn = 0.23, sample #5 and #11), the trends of measured curves are significantly different from the refractive index of MnO, and the refractive index is also sensitive to dew point. This implies the formation of distinct oxide species at different dew points. It is important to appreciate, however, that ellipsometry measurements are interpreted assuming that the oxide exists as a thin

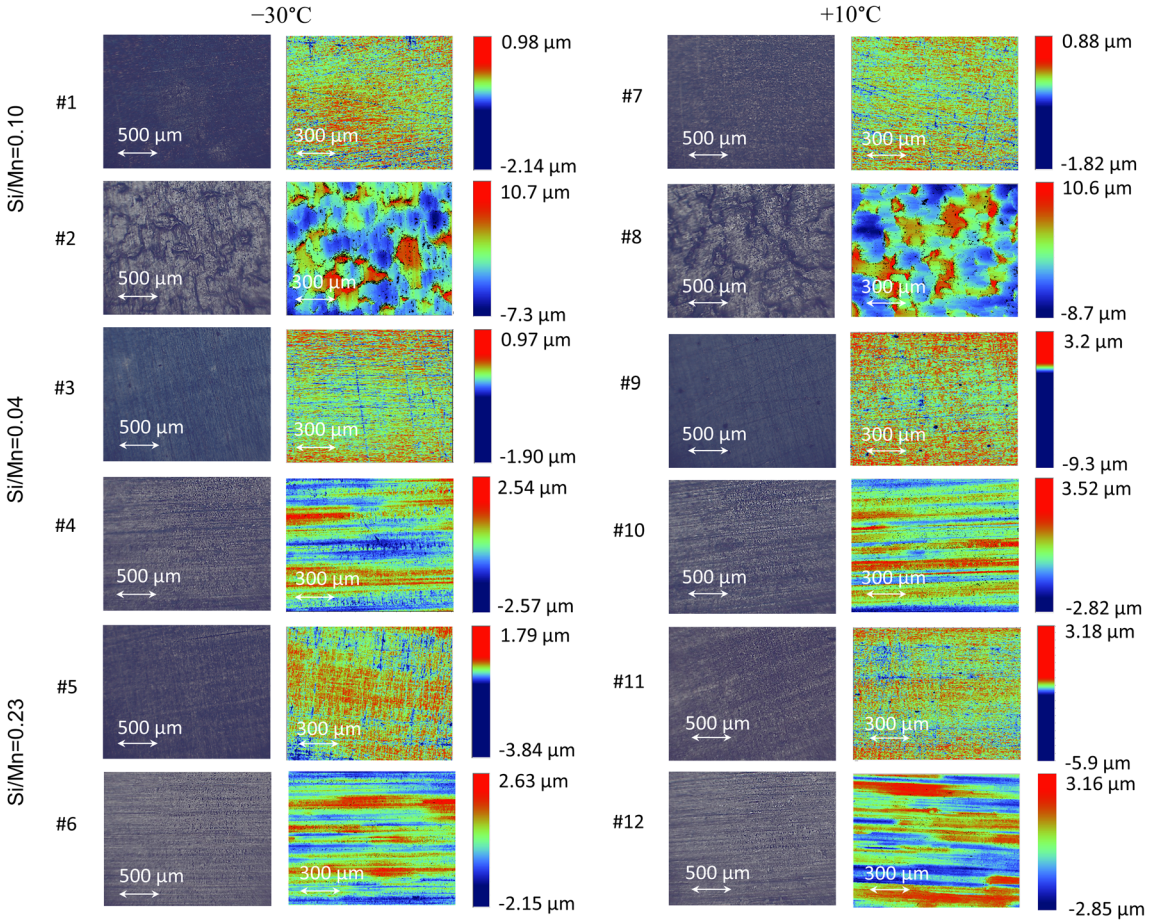

Fig. 6—Optical microscopy and optical profilograms of the samples. Samples annealed in a polished state (sample #1, #3, #5, #7, #9, #11) have similar appearance, while artifacts from the cold-rolling process are evident in sample #2, #4, #6, #8, #10, #12. Note that samples #4, #6, #10, #12 underwent ground rolling in the last stand rolling finish, and appear different from sample #2 and sample #8, which underwent electro-discharge (EDT) rolling in the last stand. Overall, samples with identical Si/Mn share a similar color and brightness attributed to oxide speciation obtained during annealing. For polished substrates, samples annealed at low dew points (− 30 °C) appear darker compared to those annealed at high dew points (+ 10 °C).

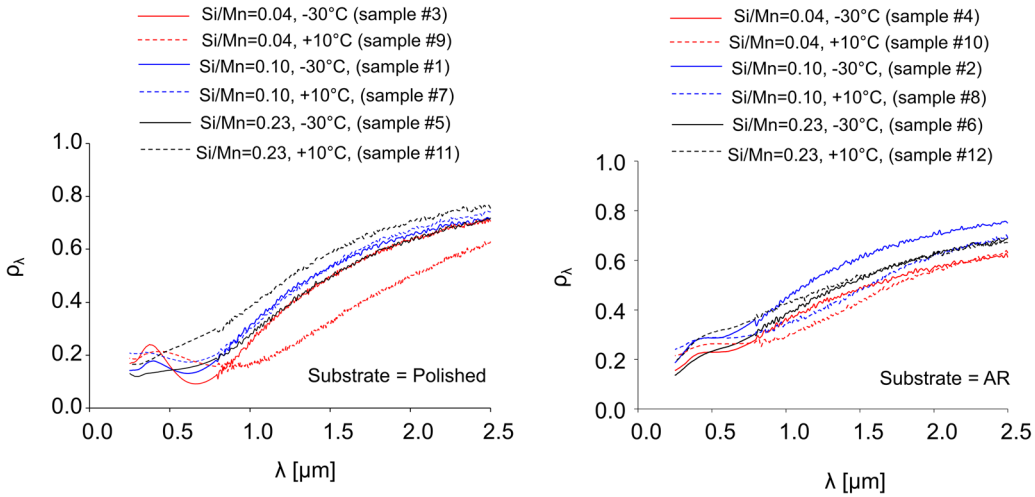

Fig. 7—Comparisons of measured directional-hemispherical reflectances for samples annealed in their polished (left) and as-received (right) states. The thin-film interference effect is more pronounced on the samples annealed in their polished state.

film; accordingly, the refractive indices for the Si/Mn = 0.23 samples, shown in Figure 9(a), should be interpreted with some skepticism.

In summary, as revealed in Figure 6, the alloy composition and surface topography have a greater impact on radiative properties of AHSS in the visible spectra compared to that of the annealing atmosphere. This is because the alloy composition, in addition to changing the surface oxide morphology, determines the oxide species having distinct refractive indices formed during annealing, as shown in Table II and Figure 9, which impacts the radiative properties. The pre-annealed surface significantly affects the EM wave interference reflections due to different levels of uniformity of oxide layers between the polished and as-received surfaces. The annealing atmosphere, however, is found to have only a minor effect on the measured reflectance. This could be attributed to the fact that oxide morphology does not change significantly between the film-like and nodular-like structures for samples having identical alloy composition and pre-annealed surface states, as observed in Figure 8.

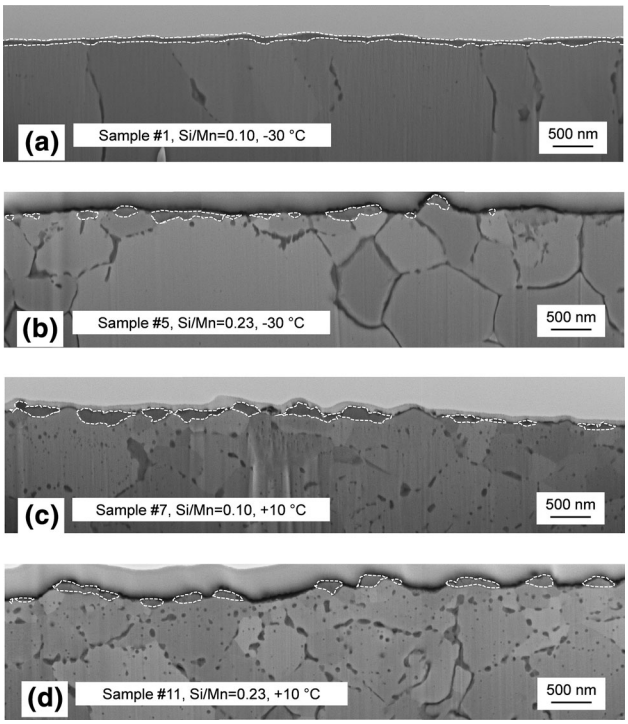

Fig. 8—Scanning electron micrographs of cross-sectional surfaces of the annealed samples. (*a*) sample #1, (*b*) sample #5, (*c*) sample #7, and (*d*) sample #11. Oxides are outlined by the white dashed lines. Sample 1 has a film-like oxide, while isolated nodules oxides are formed on sample #5 and #11. The oxide structure of sample #7 shares characteristics of both a nodular and film-like structure, but more inclined toward film-like. Oxide formations of sample #3, #9 (not shown) are film-like.

Figure 10 compares the reflectance measurements and model predictions over the UV–Vis–NIR spectra for all the polished samples. Since the thin-film interference model only applies to a smooth substrate and oxide layer, comparisons are only made using polished samples. For samples having low Si/Mn (sample #3, sample #9), the thin-film interference predictions using the refractive indices of MnO from the literature can be made within a large spectrum (0.25 to 2.5 μm) since the refractive indices of MnO from the literature cover this wavelength range. In the case of samples having more complex oxide species, the thin-film interference predictions using the measured refractive indices are limited to the visible spectrum because the ellipsometry measurements can only be done within this wavelength range using the equipment available. For all tested samples, the thin-film interference model using ellipsometry-derived oxide refractive indices over visible spectra (0.4 to 0.75 μm) is consistent with the measurements, even though the predicted refractive indices slightly underestimate the measured values. This can be attributed to the slight roughness of these polished surfaces that scattered the light away from the specular directions when carrying out the ellipsometry measurements. Accordingly, the intensities of reflected light received by the ellipsometry detector may be lower than the actual value.

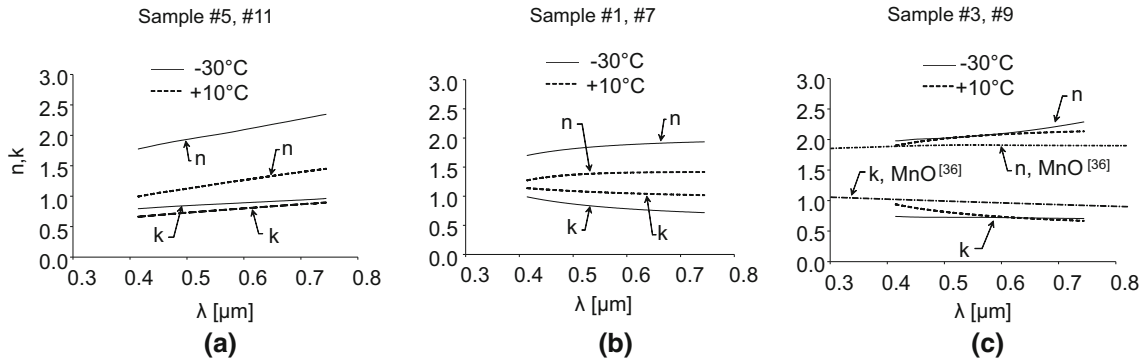

Fig. 9—Measured refractive indices of oxide film *via* ellipsometry are shown for (*a*) Si/Mn = 0.23, (*b*) Si/Mn = 0.10, and (*c*) Si/Mn = 0.04 for the samples annealed in a polished state. The solid and dash curves in the plots represent samples annealed at – 30 °C and + 10 °C atmosphere, respectively. The long-short dash lines in (c) are derived from Ref. [36]. The refractive indices shown in (a) should be interpreted with some skepticism, since the oxide has a nodular as opposed to a film-like morphology.

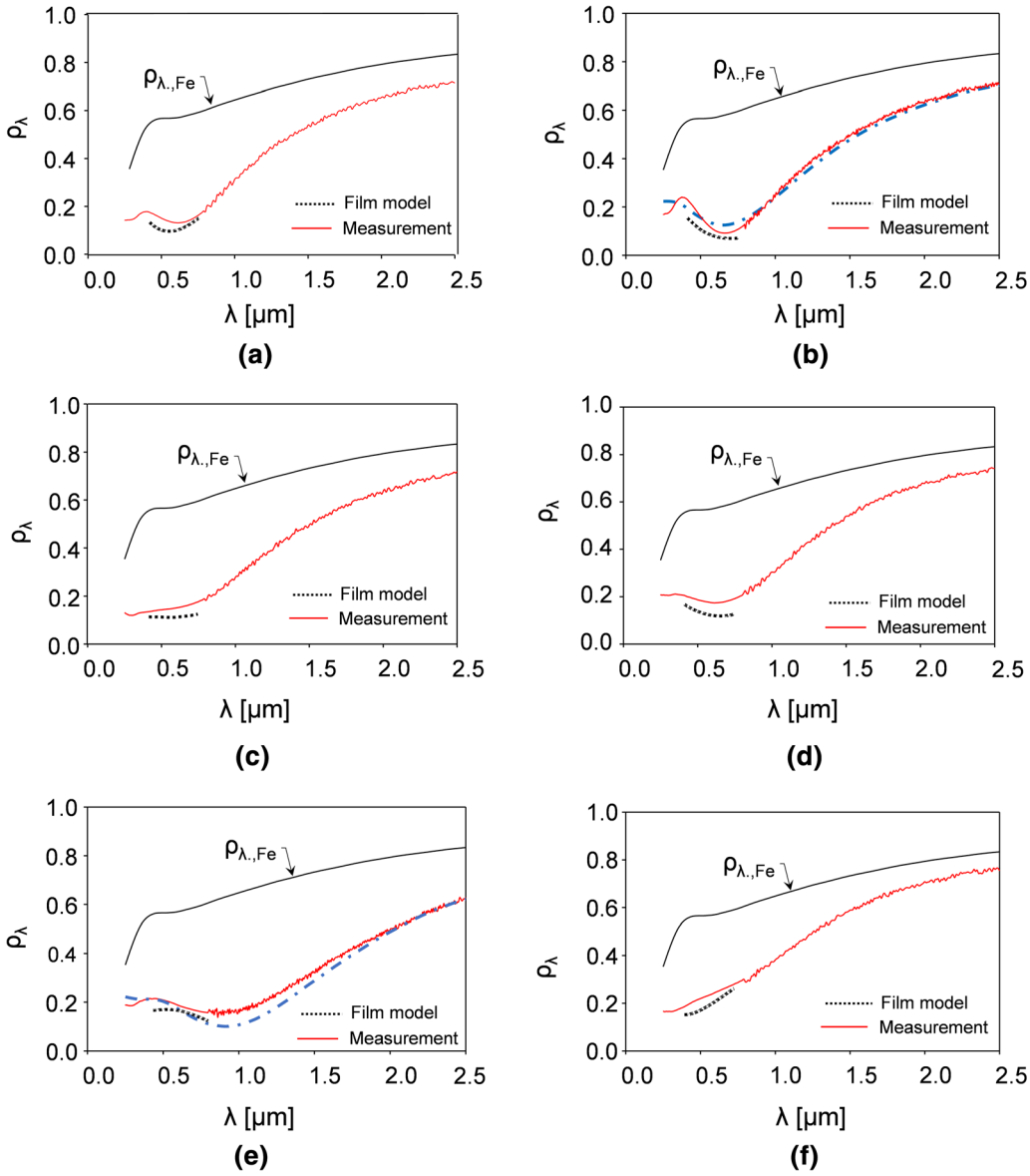

Fig. 10—Comparisons of measured and predicted reflectances for samples annealed in their polished state: (*a*) sample #1, (*b*) sample #3, (*c*) sample #5, (*d*) sample #7, (*e*) sample #9, and (*f*) sample #11. The black solid curves in the plots represent reflectance of ferrite derived using Fresnel's equation. The red curves and black dotted curves represent measurements and predictions using the thin-film interference model with measured refractive indices, respectively. The blue dashed curves in (b) and (e) denote predictions via the thin-film interference model with refractive indices of MnO obtained from Ref. [36] (Color figure online).

When the EM wavelength is comparable to the film thickness, the radiative properties of oxidized steels are influenced by both the oxide film and surface topography.[19,38] It can be seen from Figure 4 that the measured reflectance approaches the reflectance of ferrite as the wavelength increases and the surface becomes optically smooth. This implies that the radiative properties are less affected by the oxide film as the EM wavelength becomes much longer than the film thickness. For samples #3 and #9, which have the lowest Si/Mn ratio (Si/Mn = 0.04) in Figures 10(b) and (e), one can see the predictions using the thin-film interference model with MnO refractive indices from Reference 36 (blue dashed lines) also match with the measurements over the entire spectra. An obvious interference effect can be observed in Figures 10(a), (b), (d), and (e) for samples having low Si/Mn ratio (Si/Mn = 0.04, Si/Mn = 0.10).

Notably, neither sample #5 nor sample #11, Figures 10 (c) and (f), exhibit an oscillation due to thin-film interference, even though they were polished prior to annealing. As previously noted, the oxides on these samples are nodular as opposed to a homogeneous film as shown in Figure 8. Nevertheless, the thin-film model predictions are still close to the measurements. Given the fact that the refractive indices in Figure 9 are inferred from ellipsometry measurements using the thin-film interference model, it is not a surprise that incorporating the ellipsometry-measured optical

properties (oxide film refractive indices, thickness) into the thin-film interference model can reproduce a spectral reflectance in line with the measurement, even though the thin-film interference model should not be applied to a nodular oxide morphology. Accordingly, for samples having high Si/Mn, a model accounting for both the nodular oxide morphology and the roughness effect is needed to effectively predict the reflectance.

Overall, these results indicate that for AHSS samples having a polished pre-annealed surface and low Si/Mn, the effect of surface oxidation on radiative properties can be interpreted using the thin-film interference model.

VI. CONCLUSIONS AND FUTURE WORK

This study examines the effect of alloy composition, annealing atmosphere, and pre-annealed surface states on radiative properties of dual-phase steels. Thin-film interference effects are observed in the spectral reflectances of samples annealed in a polished and as-received surface state, although the effect is more pronounced for the polished samples, since the uniformity of the surface leads to more coherent wave interference effects. In the case of samples annealed in a polished state, the smoothness of the substrate and uniformity of the oxide layer permits a quantitative analysis using a thin-film interference model. XPS measurements have revealed that Mn-rich oxide (MnO) was primarily formed on those low Si/Mn alloys, while ternary oxides were found on high Si/Mn alloys. Thin-film interference effects are notably absent from two of the polished samples having high Si/Mn alloys, which had a nodular as opposed to film-like oxide morphology.

Ellipsometry measurements carried out on these samples reveal thicknesses consistent with values obtained through electron microscopy, and refractive indices that depend on the alloy composition and dew point of the annealing atmosphere. For samples having a low Si/Mn ratio (Si/Mn = 0.04), the refractive indices matched published values for MnO at both dew points, suggesting that the oxide layer consists primarily of MnO, which is consistent with the XPS measurements. Alloys having a greater silicon content showed refractive indices distinct from those of MnO and were also sensitive to dew point, due to the formation of more complex ternary oxides. In all cases, substituting the refractive indices and oxide thicknesses into the thin-film interference model produced modeled spectral reflectances that closely match those measured using a spectrometer/spectrophotometer and integrating sphere, although the validity of this approach is questionable for the high Si/Mn samples having a nodular morphology.

Future work will be focused on developing a hybrid model that accounts for both roughness and interference effects, and non-uniform oxide profile on substrate surface, which is needed to predict and interpret the radiative properties of AHSS strip in an industrial setting. Also, the refractive indices of the more complex oxides that form, particularly for high Si alloys, are not available in the literature, and thus must also be characterized in order to interpret the radiative properties of industrially relevant alloys that undergo selective oxidation during annealing.

ACKNOWLEDGMENTS

This research was supported by the Natural Sciences and Engineering Research Council Canada (NSERC CRDPJ-521291-2017 and RGPIN-2019-06535) and the International Zinc Association. The authors would like to thank Dr. Bayindir Zeynel at the Biointerfaces Institute at McMaster University for assistance with the XPS analysis, as well as Dr. Frank Goodwin (IZA), Mr. Christopher Martin-Root (Stelco), Dr. Joyce Niederinghaus (AK Steel), Mr. Michel Dubois (CMI), and Professor Myriam Brochu (Ecole Polytechnique du Montreal) for helpful discussions. The authors would also like to thank Dr. Roohen Tarighat and Dr. Hrilina Ghosh for their help with the ellipsometry measurements, and to Dr. Yuquan Ding for his help with the profilometry measurements.

DATA AVAILABILITY

The raw/processed data required to reproduce these findings cannot be shared at this time as the data also forms part of an ongoing study.

REFERENCES

1. R.G. Thiessen, E. Bocharova, D. Mattissen, and R. Sebald: *Metall. Mater. Trans. B*, 2010, vol. 41B, pp. 857–63.
2. Q. Somveille, P. Mosser, M. Brochu, K.J. Daun, *Galvatech 2017*, pp. 210–17.
3. S.H. Ham, C. Carteret, J. Angulo, and G. Fricout: *Corros. Sci.*, 2018, vol. 132, pp. 185–93.
4. C. Shi, K.J. Daun, and M.A. Wells: *Int. J. Heat Mass Transf.*, 2015, vol. 91, pp. 818–28.
5. R. Brannon and R.J. Goldstein: *J. Heat Transf.*, 1970, vol. 92 (2), pp. 257–63.
6. R. Khondker, A. Mertens, and J.R. McDermid: *Mater. Sci. Eng. A*, 2007, vol. 463 (1–2), pp. 157–65.
7. H. Liu, Y. He, S. Swaminathan, M. Rohwerder, and L. Li: *Surf. Coat. Technol.*, 2011, vol. 206 (6), pp. 1237–43.
8. E. Bellhouse, J.R. McDermid, in: *Proc. Materials Science and Technology Conf. and Exhib*, 2009, pp. 913–24.
9. M. Pourmajidian, B. Langelier, and J.R. McDermid: *Metall. Mater. Trans. A*, 2018, vol. 49A, pp. 5561–73.
10. F.K. Suleiman, K. Lin, K.J. Daun, *J. Quant. Spectrosc. Radiat. Transf.*, 2021, pp. 107693.
11. T. Iuchi, T. Furukawa, and S. Wada: *Appl. Opt.*, 2003, vol. 42 (13), pp. 2317–26.
12. L. de Campo, R.B. Pérez-Sáez, X. Esquisabel, I. Fernández, and M.J. Tello: *Rev. Sci. Instrum.*, 2006, vol. 77 (11), p. 113111.
13. J.R. Howell, M.P. Mengüç, K.J. Daun, and R. Siegel: *Thermal Radiation Heat Transfer*, CRC Press, Boca Raton, 2020.
14. K. Lin and K.J. Daun: *J. Quant. Spectrosc. Radiat. Transf.*, 2020, vol. 242, p. 106796.
15. K. Lin, F.K. Suleiman, and K.J. Daun: *Int. J. Heat Mass Transf.*, 2021, vol. 176, p. 121429.
16. G. Neuer and F. Güntert: *Thermochim. Acta*, 1988, vol. 133, pp. 299–304.

17. M. Kobayashi, M. Otsuki, H. Sakate, F. Sakuma, and A. Ono: *Int. J. Thermophys.*, 1999, vol. 20 (1), pp. 289–98.
18. L. Del Campo, R.B. Perez-Saez, and M.J. Tello: *Corros. Sci.*, 2008, vol. 50 (1), pp. 194–99.
19. J. King, H. Jo, R. Tirawat, K. Blomstrand, and K. Sridharan: *Nucl. Technol.*, 2017, vol. 200 (1), pp. 1–14.
20. A.E. Morris, G. Geiger, and H.A. Fine: *Handbook on Material and Energy Balance Calculations in Material Processing*, Wiley, New York, 2012.
21. G.S. Mousavi and J.R. McDermid: *Metall. Mater. Trans. A*, 2018, vol. 49A, pp. 5546–60.
22. G.S. Mousavi, B. Langelier, and J.R. McDermid: *Metall. Mater. Trans. A*, 2019, vol. 50A, pp. 2898–2911.
23. E. Bellhouse and J.R. McDermid: *Mater. Sci. Eng. A*, 2008, vol. 491 (1–2), pp. 39–46.
24. E. Bellhouse and J.R. McDermid: *Metall. Mater. Trans. A*, 2010, vol. 41A, pp. 1539–53.
25. E.M. Bellhouse, A. Mertens, and J.R. McDermid: *Mater. Sci. Eng. A*, 2007, vol. 463 (1–2), pp. 147–56.
26. Y.F. Gong, H.S. Kim, and B.C. De Cooman: *ISIJ Int.*, 2009, vol. 49 (4), pp. 557–63.
27. L. Cho, S.J. Lee, M.S. Kim, Y.H. Kim, and B.C. De Cooman: *Metall. Mater. Trans. A*, 2013, vol. 44A, pp. 362–71.
28. L. Cho, G.S. Jung, and B.C. De Cooman: *Metall. Mater. Trans. A*, 2014, vol. 45, pp. 5158–72.
29. Y. Suzuki, T. Yamashita, Y. Sugimoto, S. Fujita, and S. Yamaguchi: *ISIJ Int.*, 2009, vol. 49 (4), pp. 564–73.
30. M.C. Rey, D.P. Kramer, W.R. Henderson, L. Abney, *Monsanto Research Corp.*, 1984.
31. M. Pourmajidian and J.R. McDermid: *Metall. Mater. Trans. A*, 2018, vol. 49A, pp. 1795–1808.
32. S. Alibeigi, R. Kavitha, R. Meguerian, and J.R. McDermid: *Acta Mater.*, 2011, vol. 59 (9), pp. 3537–49.
33. J. Oh, L. Cho, M. Kim, K. Kang, and B.C. De Cooman: *Metall. Mater. Trans. A*, 2016, vol. 47A, pp. 5474–86.
34. M.Q. Brewster: *Thermal Radiative Transfer and Properties*, Wiley, New York, 1992.
35. M. Querry, *Optical constants*, contractor report, US Army Chemical Research, Development and Engineering Center, 1985, p. 418.
36. J. Hugel and C. Carabatos: *Solid State Commun.*, 1986, vol. 60 (4), pp. 369–72.
37. Standard ASTM A1079-17, 2017.
38. K. Tang, P.A. Kawka, and R.O. Buckius: *J. Thermophys. Heat Transf.*, 1999, vol. 13 (2), pp. 169–76.
39. Q. Zhu, H. Lee, and Z. Zhang: *J. Thermophys. Heat Transf.*, 2005, vol. 19 (4), pp. 548–57.